Research Article Vol. 33, No. 11 / 2 Jun 2025 / *Optics Express* 22755

Optics EXPRESS

Stereo hard X-ray ptychography

Sina Röper,[1,2,*] Sarah-Alexandra Hussak,[1,2] Karolina Stachnik,[2] Dorota Koziej,[2] Mattias Åstrand,[3] Ulrich Vogt,[3] Caterina Carus,[1,4] Johannes Dora,[1,5] Johannes Hagemann,[1] Martin Seyrich,[1] Christian G. Schroer,[1,4] and Andreas Schropp[1,6]

[1] *Centre for X-ray and Nano Science CXNS, Deutsches Elektronen-Synchrotron DESY, Notkestraße 85, 22607 Hamburg, Germany*
[2] *Center for Hybrid Nanostructures, Institute for Nanostructure and Solid-State Physics, University of Hamburg, Luruper Chaussee 149, 22761 Hamburg, Germany*
[3] *KTH Royal Institute of Technology, Department of Applied Physics, Biomedical and X-ray Physics, Albanova University Center, 106 91 Stockholm, Sweden*
[4] *Department Physik, Universität Hamburg, Luruper Chaussee 149, 22761 Hamburg, Germany*
[5] *Institute for Biomedical Imaging, University of Technology Hamburg TUHH, Lottestraße 55, 22529 Hamburg, Germany*
[6] *Helmholtz Imaging, Deutsches Elektronen-Synchrotron DESY, Notkestraße 85, 22607 Hamburg, Germany*
[*] *sina.roeper@xray-lens.de*

Abstract: Hard X-ray ptychography has strongly developed during the last decade, enabling one to visualize structural properties of materials at high spatial resolution. By combining it with multi-slicing or tomographic techniques, optically thick samples can be investigated in 3D. Nevertheless, the depth resolution in multi-slicing is often limited to several micrometers by the ptychographic optical system and a full laminographic or tomographic investigation may be hindered by experimental constraints of limited space or acquisition time. Here, we introduce a stereoscopic imaging system using two inclined nanofocused X-ray beams to illuminate a sample at varying angles at the same time. Similar to human vision, adding these stereoscopic views results in considerably improved in-depth resolution beyond the current limits of pure 2D imaging systems. This is especially promising for experimental applications requiring bulky sample environments.

1. Introduction

Microscopy plays a crucial role in various scientific fields, providing insight into the structure and functioning of materials on multiple length scales. While transmission electron microscopy can reach atomic resolution on small samples with a thickness of typically below 1 µm [1], hard X-ray microscopy can be applied in the case of larger and thicker samples due to its higher penetration depth. The latter becomes even more important if measurements are to be carried out under special *in-situ* or *operando* conditions in order to better reproduce a real operating environment. Therefore, hard X-ray microscopy is a powerful method for structure determination in three dimensions that is applied in many scientific fields, such as biology, chemistry, physics, materials science and nanotechnology [2,3].

Hard X-ray microscopy has the unique strength that the internal structure of thick samples can be investigated with high spatial resolution, which has even been pushed beyond the limits of current X-ray optics by scanning coherent X-ray microscopy (ptychography) in the past two decades [4–8]. To obtain a three-dimensional impression, most imaging techniques require a full

#559273 https://doi.org/10.1364/OE.559273
Journal © 2025 Received 18 Feb 2025; revised 8 May 2025; accepted 13 May 2025; published 23 May 2025

rotation of the sample, and different 3D ptychographic imaging experiments have been carried out in tomographic or laminographic scanning mode [9–11]. Alternatively, 3D information of a sample can also be obtained by multi-slice ptychography. In this case, the depth information is extracted from just a 2D scan, which requires that variations in the illumination function are sufficiently large such that different sample layers can be separated from each other [12–14].

This also enables imaging of optically thick samples. However, depth information in multi-slice ptychography can only be obtained for samples thicker than the depth of field of the imaging system [14,15]. Acquisition of multiple projections can overcome this limitation. This was achieved with sequential stereoscopic X-ray ptychography by rotation of the sample [16–18]. A separation in multi-slice reconstruction of slices thinner than the depth of field of the imaging system was demonstrated using nine scans of the sample tilted by 1° around four axes [19,20]. However, the need for rotation of the sample increases the necessary scan time. Simultaneous acquisition of multiple projections of a sample is especially valuable for *in-situ* or *operando* studies, where a high temporal resolution is crucial. For single shot ptychography, multi-slicing was realized with multiple inclined laser beams [21,22]. The simultaneous measurement of multiple projections with hard X-rays was accomplished with a resolution in the micrometer range [23–26]. In the field of high-resolution X-ray microscopy, stereoscopic or multi-projection X-ray imaging was demonstrated for coherent diffractive imaging at X-ray free electron lasers [27–30]. At synchrotron sources, simultaneous microscopy of multiple projections was shown for propagation-based phase-contrast imaging [29], differential phase imaging [31], and holotomography [32]. Another option to speed up the acquisition of volumetric ptychographic data sets is the use of multi-beam ptychography [33–38], which in principle could be combined with a rotation of the sample.

The simultaneous acquisition of multiple X-ray ptychographic projections has not been demonstrated so far. Our experiment is the first of its kind in this regard and makes use of the qualities of hard X-ray ptychography to offer the potential for a lateral resolution of 10 nm [39,40]. Meanwhile, it is suitable for a variety of samples ranging from bacteria [39,41] to *in-situ* studies of chemical systems [42–44].

2. Stereoscopic X-ray microscopy

Similar to human vision, multiple perspectives of a sample can provide a considerably improved 3D depth perception. In the presented case, the stereoscopic X-ray impression is created by two separate nanofocused X-ray beams that illuminate a sample with a certain angular offset. The beams are produced by a set of X-ray optics, as illustrated in Fig. 1. The direct, middle beam facilitates the alignment of the setup.

The focal length of the Fresnel zone plates (FZPs) and the optimal reflection angle of the small multilayer (ML) mirrors are chosen such that the three beams overlap close to the focal plane of the FZP optics. By positioning a diffraction detector in the far-field regime of the imaging system, three individual ptychographic data sets can be recorded at the same time, each capturing a distinct view of the sample. The strongest stereoscopic effect can be expected from the outermost two beams, because of the maximum deflection angle, but in practice any two-beam combination from the setup can be used for stereoscopic vision.

2.1. Depth resolution in stereo microscopy

Stereoscopic ptychography allows for a visual depth resolution well below the limits of conventional ptychography. For multi-slice ptychography, the minimal slice distance d_p was defined with numerical simulations as

$$d_p \geq 5.2\frac{\delta^2}{\lambda}, \tag{1}$$

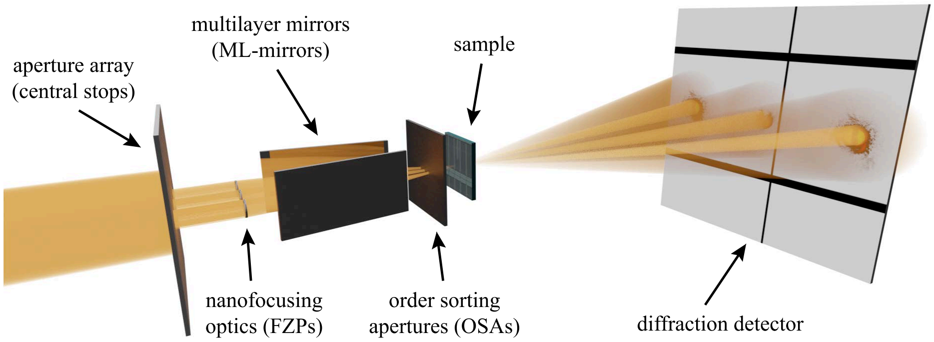

Fig. 1. Schematic of the stereoscopic X-ray imaging setup. Three beams are formed by an aperture array that includes central stops and are then focused by a set of Fresnel zone plates (FZPs). The outer two beams are subsequently deflected by two multilayer-mirrors (ML-mirrors).

where λ and δ denote the wavelength and the lateral spatial resolution, respectively [13]. Theoretical considerations based on the maximum detected scattering angle led to a similar definition with the constant being 4.88 instead of the 5.2 [45].

For stereoscopic ptychography, the depth resolution does not rely on propagation effects of the illuminating wave field. The depth resolution in stereo imaging can be defined based on ray tracing of the beams through the sample (see Fig. 2). Therefore, the limit can be defined by s, the minimal transverse shift required of the two beams with respect to each other, as $s>\delta$ with $s = 2d_s \cdot \tan(\theta_s)$, where θ_s is the deflection angle of a single beam of the stereo setup.

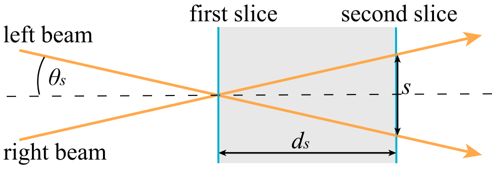

Fig. 2. Schematic of the two deflected beams passing through two slices of a sample. The angle between the two beams is $2\theta_s$, the shift between the two beams in the second slice s, and the distance between the slices d_s. To see a difference of the layers in depth the shift s has to be greater than the lateral resolution δ.

For small angles between the deflected beams, the minimal slice distance can be defined as

$$d_s > \frac{\delta}{2\theta_s}, \tag{2}$$

where d_s now defines the axial resolution. This definition is in good agreement with the depth resolution defined by Duarte, *et al.*, for stereoscopic coherent diffractive imaging: $d_s = \delta/(\tan\theta_1 + \tan\theta_2)$, where θ_1 and θ_2 are the angles of the deflected beams with respect to the optical axis [27].

2.2. X-ray optics

Our stereoscopic microscope is mainly based on a set of FZPs and flat ML-mirrors. The ML-mirrors had a length of 12 mm, which is small enough for them to be positioned between the FZPs and the focal plane of the optics (see Fig. 3).

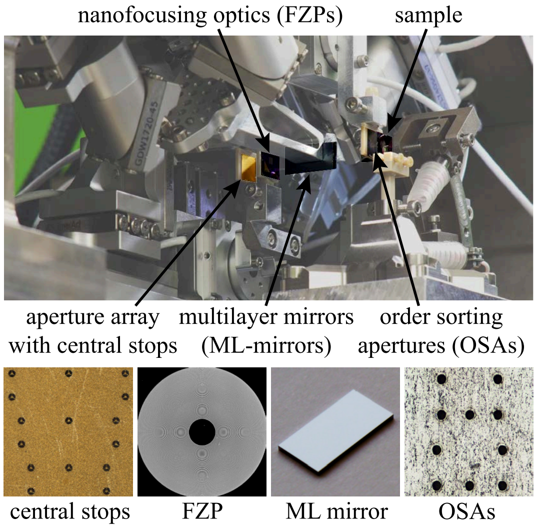

Fig. 3. Photo of the stereo setup implemented into PtyNAMi highlighting the different X-ray optics used, namely: an array of central stops, the FZPs for focusing, the ML mirrors to deflect the X-ray beams and an array of order sorting apertures (OSAs) to clean the focused beam from undesired diffraction orders of the FZPs.

The three nanobeams were created by introducing first an array of apertures with integrated central beam stops that are required to block the zeroth order of the FZPs. The gold central stops had a diameter of 25 µm and a thickness of 40 µm. Subsequently, the three separate parts of the X-ray beam were focused by a set of FZPs. They were laterally displaced in the horizontal direction by 500 µm, meaning that the individual beams can be considered as mutually incoherent. The FZPs were fabricated out of gold via a direct-write electron-beam lithography process followed by electroplating [46,47], with a diameter of $D = 74.9$ µm and an outermost zone width of $d_n = 60$ nm. The small W/Si-ML-mirrors were produced by AXO DRESDEN GmbH, Germany with alternating layers of tungsten and silicon with a period thickness of 6.4 nm. A mask with order sorting apertures (OSAs) was positioned between the mirrors and the sample to filter out all undesired diffraction orders of the FZPs. The mask was made out of a 50 µm thick tungsten foil. Individual apertures had a diameter of 17.5 µm.

2.3. Implementation into PtyNAMi

The different X-ray optics were implemented into the ptychographic nano-analytical microscope (PtyNAMi) [48]. This instrument at beamline P06 at PETRA III (DESY Hamburg, Germany) provides all degrees of freedom to align the optics with the required positioning stability and accuracy. Due to rather strong space constraints, as shown in Fig. 3, the optics were implemented using a compact set of different stages and hexapods (SmarAct GmbH, Germany) for their precise alignment.

In this experiment, the X-ray photon energy was set to $E = 8.0$ keV by a silicon channelcut monochromator. At this energy we expected a diffraction-limited beam spot from the FZPs of $d = 1.22 d_n \approx 73$ nm at a focal length of $f_1 = D d_n / \lambda = 29$ mm. The ML-mirrors had a maximum reflectance of $R = 80\%$ at the Bragg angle of $\vartheta = 0.75^\circ$. Hence, the deflection angle of a single mirrored beam was $\theta = 2\vartheta = 1.5^\circ$ with respect to the forward direction and the maximum viewing angle between the two outermost nanobeams was therefore $2\theta = 3.0^\circ$.

We observed three separated beams on the detector at a distance of $L = 2.0$ m from the sample, as indicated in Fig. 4. The diffraction patterns were recorded by an Eiger X 4M photon counting detector (DECTRIS AG, Switzerland) with a pixel size of 75 µm positioned at the end of an evacuated flight tube. The separation between the different beams was sufficiently large so that each signal could be analyzed individually and the spurious diffraction signal from a neighboring beam could be neglected. More specifically, 712 pixels between two beams correspond to a distance of 53.4 mm on the detector, or an angle of 1.53°, which is very close to the theoretically expected value of $\theta = 1.5^\circ$ (see Fig. 4). To accommodate all three beams on the detector, it has to be positioned closer to the sample than in single-beam ptychography. This leads to a lower sampling of the diffraction patterns and, depending on the size of the illumination, may reduce the reconstruction quality. In the present case, the stereographic data were reconstructed with an upsampling factor of 2 to mitigate this effect of a slightly reduced data sampling in reciprocal space [49].

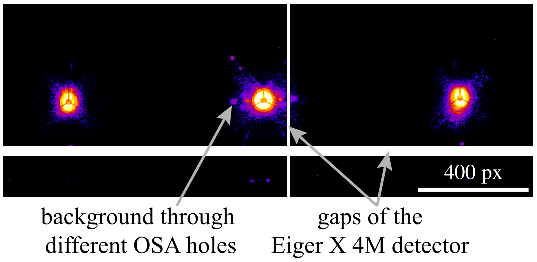

Fig. 4. Three distinct far-field diffraction patterns, measured simultaneously on the Eiger X 4M detector at $L = 2$ m distance from the sample.

The spatial resolution is limited by the maximum scattering angle that can be cropped out from the detector image for each individual diffraction pattern. In the current stereo-imaging geometry, using in addition the central third beam, this yields an area on the detector of about 512 × 512 pixels for each of the individual nanofocused X-ray beams. It guarantees that there is no overlap between adjacent diffraction patterns on the detector. At the chosen exposure times and cropping areas we did not observe a significant crosstalk between the different nanofocused X-ray beams. The individual ptychograms can therefore be treated like normal single-beam scans without compromising reconstruction accuracy. Without the central X-ray beam and if the detector size is sufficiently large, the cropping area could in principle be increased, thereby further enhancing the maximum achievable spatial resolution for the different stereoscopic perspectives. A photon-counting detector with a large detection area can ensure a high signal-to-noise ratio and detection efficiency also at high scattering angles. The inclination angle of 1.5° for the two outermost beams on the detector is negligible as it is associated with a reduction in the horizontal size of the detection area of only 0.03 % compared to the perpendicular geometry.

Setting up the stereo X-ray microscope requires a precise alignment of the X-ray optics such that the different nanobeams overlap in the sample plane and is therefore more time consuming. Here, the standard configuration of PtyNAMi could be employed to a large extent, thereby reducing setup time to a minimum. However, optimization of the setup or ideally a dedicated endstation would allow to reduce the additional time needed. The X-ray beam, provided by PETRA III, was quite stable throughout the experiment and we did not experience any increased influence of X-ray beam instabilities on the reconstruction quality. If a comparable setup would be used at, e.g., X-ray free-electron lasers, one would have to re-evaluate this.

The logic structure of an STM32H753VIT6 microcontroller (STMicroelectronics, Switzerland) with an Arm Cortex-M7 core was used as the sample for the experimental demonstration of stereo ptychography. Microchips are produced layer-wise by lithography techniques and, hence, have a three dimensional structure, which can be well observed with stereoscopic microscopy. The microchip was scanned over a quadratic area of 30 µm × 30 µm in 100 × 100 steps, whereby an additional random jitter of up to 30 % of the step size was added to the nominal positions in order to prevent scanning on a perfect 2D grid in ptychography [50]. The mean step size was therefore 300 nm and, additionally, optical interferometers tracked the sample position for every scan point. The non-deflected central beam defined the optical axis of the microscope and considerably facilitated the alignment of all optical components.

Figure 5 shows the reconstructed ptychographic image of the microchip obtained using the diffraction patterns only from the central beam.

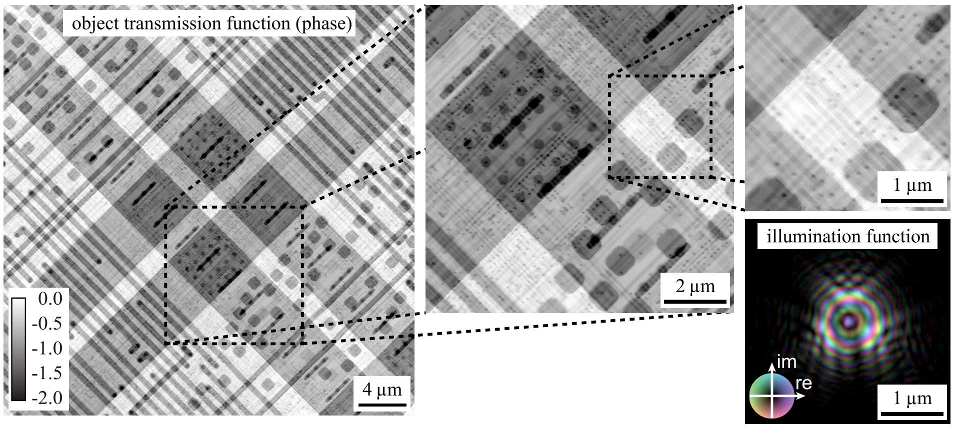

Fig. 5. Ptychographic reconstruction of the microchip sample using the central beam only. It highlights the large field of view of 30 µm and the high spatial resolution of around 14 nm, with fine structural details shown in the magnified areas. Phase shifts of the object transmission function are given in radians whereas the amplitude and phase of the complex-valued illumination function are encoded by brightness and hue, respectively (see insets).

The size of the reconstructed illumination function indicates that the sample was not scanned in the focal plane of the optics but rather at a distance of 0.5 mm upstream. This permitted to perform the ptychographic scan with a larger step size due to the extended illuminating wave field.

The focus size of the optics was determined to about 70 nm (FWHM) by numerically propagating the retrieved complex-valued illumination function into the focal plane of the optics. The depth of focus of the FZP optics is given by $d_\text{o} = \lambda/(2\text{NA}^2) \approx 50$ µm in this case. However, in ptychography neither the lateral nor the axial resolution are limited by the optics but rather by the maximum diffraction angles at which a significant diffraction signal can be measured [45]. Here, the spatial resolution in the 2D ptychographic image was determined by Fourier-ring correlation to $\delta = 14$ nm (see Supplement 1 Fig. S1), which considerably improves also the axial resolution in this single-view ptychographic scan to below $d_\text{p} \approx 7$ µm using Eq. (1).

3. Stereoscopic X-ray vision

The same region was scanned with the left and right nanofocused beams at the same time. Due to their inclination angle of maximum 1.5°, the resulting reconstructed objects exhibit subtle lateral shifts of certain features encoding their position in the layered microchip electronics' structure. From the perspective of the X-ray beams, we speak of "left" and "right" nanobeam or view, depending on whether the signal originates from the left or right side of the incident X-ray beam, similar to the notation of left and right eye.

First, the different nanobeams were characterized by ptychography and the result is summarized in Fig. 6. The ptychograms of the three nanobeams were separately reconstructed with in-house software, which is based on the ePIE algorithm [6]. The reconstructions were run with 900 iterations of the ePIE engine followed by 100 iterations of a parallel update scheme [51]. With this method, the individual sub-beams and respective projections of the sample were recovered. Since the diffraction patterns of each beam are well separated, a disentanglement, as it is necessary in multi-beam ptychography where the diffraction patterns of the beams overlap, is not needed. The total computation time is therefore comparable to the reconstruction of three single-beam ptychograms. Parallel reconstruction of the three projections on different computing nodes would even allow for reconstruction at the same speed as a single-beam ptychogram. Afterwards, the horizontal and vertical offsets between the projections were determined with the phase cross correlation function of the python library scikit-image. The offset of 13 pixels in vertical and 62 pixel in horizontal direction were corrected by translation of the individual projections.

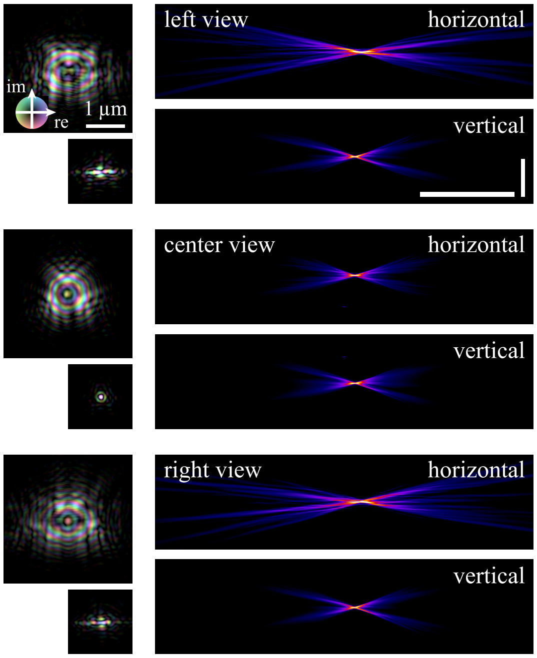

Fig. 6. Characterization of the three nanofocused X-ray beams. The complex-valued illumination functions of the three beams in the sample plane are shown on the left side of the figure. Smaller images below indicate the wave field in the focal plane of the FZP optics. The corresponding beam caustics in horizontal and vertical direction are summarized on the right side. Scale bars in the caustic images refer to 5 mm along the optical axis of the individual beams and 5 µm in the lateral direction.

As expected, comparing the beam caustics of the deflected (left and right) beams and the direct (center) beam shows that the ML-mirrors mainly alter the horizontally deflected nanofocused beams in the horizontal direction. The complex wave fields of these nanobeams exhibit a pronounced astigmatism shifting the horizontal focus by about 400 µm further downstream. These imperfections of the illuminating beams could cause difficulties for imaging techniques that in some cases rely on an ideal illumination, such as inline holography [52,53]. However, the performance of ptychography does not depend on perfect focusing conditions, since the illumination function is recovered during phase retrieval, and the imaging performance does not degrade as long as the beam size is not increased beyond the limits required for an optimal sampling of the diffraction patterns.

The reconstructions of the microchip sample scanned with the inclined beams, alongside the anaglyph of the two perspectives, are shown in Fig. 7. The anaglyph image of the aligned reconstructions allows a clear distinction between several of these layers in the sample (see Fig. 7). From the cross section of the microchip (see Fig. 8) one can see that larger structures, which appear farther back in the anaglyph, are thicker and farther spaced than smaller structures, which

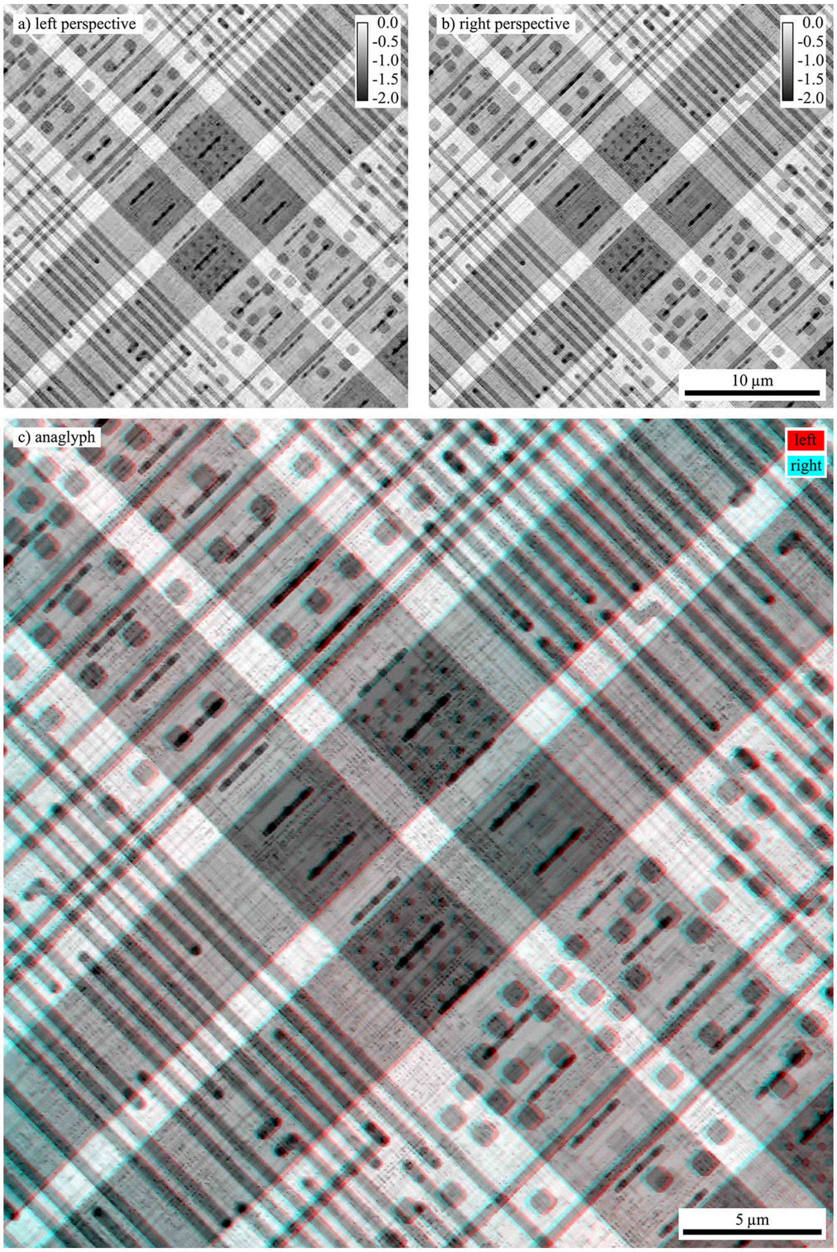

Fig. 7. Reconstructions of a stereoscopic scan of an STM32H753VIT6 microcontroller. a) shows the phase reconstructions of the sample scanned with the deflected beam that is on the left on the detector. b) is the result of scanning with the right beam at an angle of 3.0° with respect to the left beam. The anaglyph of the two projections is shown in c).

appear closer in the anaglyph. This depth perception is, as anticipated, based on the direction of the beams passing though the sample. The beams were traversing the sample from the substrate side to the side with conductor paths. Smaller features, embedded deeper in the microchip, were downstream, whereas thick conductor paths were upstream. The total thickness of the logical structure of the microchip was 3.8 µm with layer distances between 1.1 µm and less than 0.1 µm.

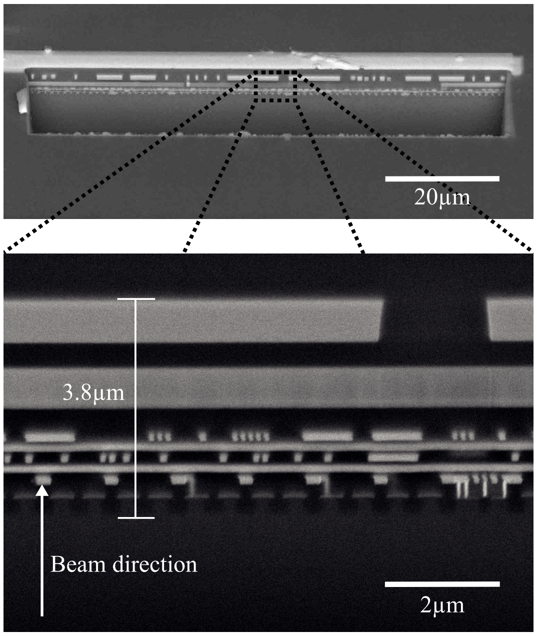

Fig. 8. Cross section of the microchip imaged with a scanning electron microscope after preparation with a focused ion beam. The X-ray beams were passing through the sample from the small features to the larger ones. The total thickness of the conductor path structures of the chip is 3.8 µm.

The resolution of the reconstructions, determined by Fourier-ring correlations, is 10 nm for the left beam and 12 nm for the right beam (see Supplement 1 Fig. S1). Therefore, as a conservative estimate of the spatial resolution in the single ptychographic reconstructions, we use the size of two pixels $\delta = 16.2$ nm and, hence, a 3D perception due to the stereoscopic effect is given for features that are separated in depth by $d_\mathrm{s} \approx 300$ nm using Eq. (2). This value is significantly lower than the minimal separation distance of layers in conventional multi-slice reconstructions, which would require a distance of $d_\mathrm{p} \approx 9$ µm according to Eq. (1). An attempt of applying multi-slice ptychography on a single-view ptychographic dataset is summarized in Fig. S3 in the Supplement 1, which shows, however, that a single perspective does not contain sufficient depth information on the required length scale. Therefore, the use of stereoscopic ptychography with a viewing angle of 3.0° improves the thickness limit for a depth impression of the sample in this case by more than one order of magnitude, allowing us to visually separate the different layers of the logic structures of the microchip.

4. Slice recovery in stereo X-ray ptychography

We demonstrate the potential of stereo X-ray ptychography to quantitatively separate tightly connected layers at the example of another specimen with a less complex layer structure. In this case, we used a silicon nitride membrane of 200 nm thickness with Au nanoparticles with a diameter of 250 nm on one side and an FZP on the other side. The scanned part of the FZP, here, acts as a sample structure and not as a focusing optic. In Fig. 9(a) a schematic drawing of the sample is shown.

This sample was scanned over an area of 4 μm × 8 μm in 20 × 40 steps, with an additional random jitter of up to 30 % of the step size. The exposure time per scan point was 0.1 s. The left and right projection were reconstructed separately with 800 iterations of the ePIE algorithm [6] followed by 200 iterations of a parallel update scheme [51]. Position refinement was used starting at iteration 650 [54]. The reconstructions were mutually aligned with a vertical shift of 186.5 px and a horizontal shift of 156.5 px and cropped to a size of 550px × 900px (4.4 μm × 7.3 μm) for the slice separation. The spatial resolution for both projections, determined by Fourier ring correlation, is 13 nm (see Fig. S2 in the Supplement 1). Similar to the microchip sample, we therefore estimate limits in depth resolution of approximately $\delta_s \approx 300$ nm.

The thickness of the FZP, which is also made of Au, can be deduced quantitatively from the ptychographic reconstruction itself, which shows an average phase shift of −0.61 rad for its Au nanostructures. At the X-ray photon energy of 8 keV and using tabulated values for the refractive

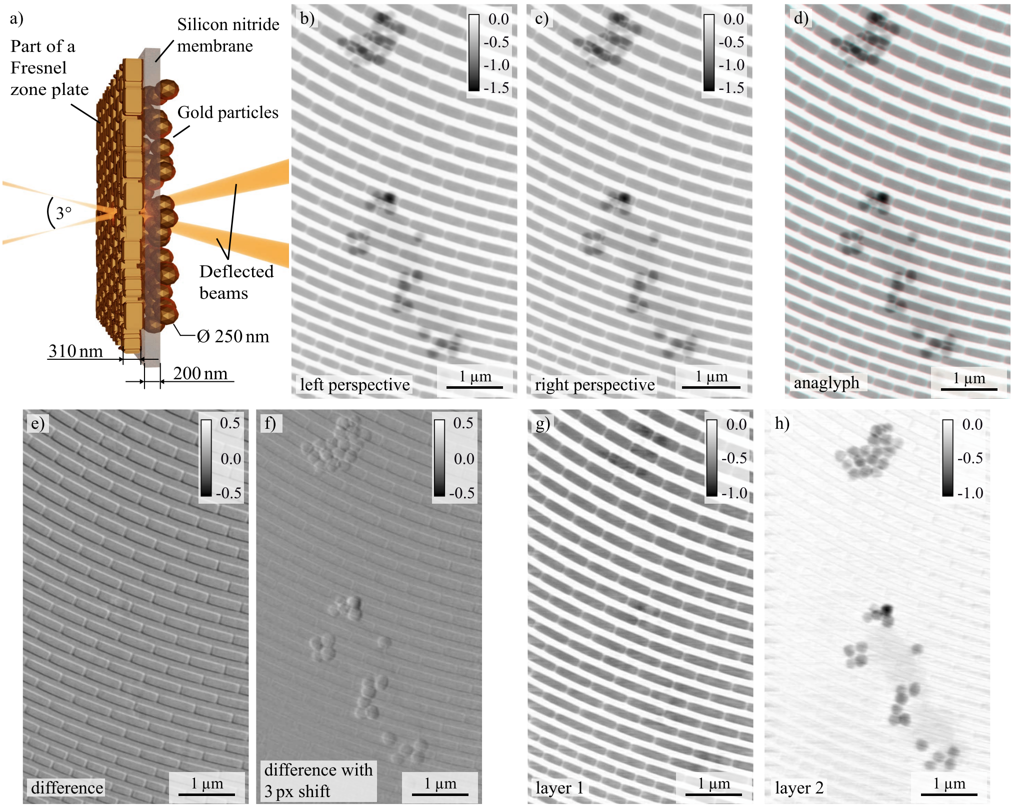

Fig. 9. Two layers separated by a 200 nm thick membrane recovered from the left and right perspective. a) shows a schematic top view of the sample: a silicon nitride membrane with a Fresnel zone plate on one side and gold nanoparticles on the other side. b) and c) show the reconstructions of the left and right beam data sets. d) is an anaglyph of the two projections. e) shows the difference of the aligned reconstructions b) and c). The reconstructions are aligned in the second slice. f) shows the difference of the reconstructions with a shift of 3 px. The projections are here aligned in the first slice. g) and h) show the two layers recovered from the two projections b) and c) with an iterative algorithm based on a relative shift of the beams in the respective layers.

index decrement of $\delta_{\mathrm{Au}} = 4.77 \cdot 10^{-5}$ [55], this translates into an FZP thickness of 310 nm. Together with the 200 nm thick silicon nitride membrane and the 250 nm Au nanoparticles, the sample has a total thickness of about 760 nm. It is thus ideal for demonstrating the enhanced depth resolution of stereo X-ray ptychography.

To separate the Au nanoparticles from the FZP, the left and right projection t_1 and t_2, respectively, are modeled as the sum of two object layers l_1 and l_2 with a lateral shift S in one of the layers:

$$\begin{pmatrix} t_1 \\ t_2 \end{pmatrix} = \begin{pmatrix} S & \mathbb{1} \\ \mathbb{1} & \mathbb{1} \end{pmatrix} \cdot \begin{pmatrix} l_1 \\ l_2 \end{pmatrix} \tag{3}$$

We numerically solve the corresponding constrained convex optimization problem. The algorithm is set up so that features in the first (upstream, l_1) layer show a shift between the left and right perspectives, while features in the second (downstream, l_2) layer remain in place. Since we assume that the displacements are constant over the entire field of view in each slice and shear is neglected, this approach is only valid for small angles and thin slices. Further implementation details of the algorithm can be found in Supplement 1. The results are summarized in Fig. 9.

A difference image of the two aligned projections (see Fig. 9(e)) reveals the contour of the FZP structures, while the Au nanoparticles are barely visible. Therefore, the layer comprising the Au nanoparticles is consistent in both projections. The distance between the FZP and the nanoparticle layer is approximately 480 nm. For an angle of 3.0° this corresponds to a relative shift of 25.1 nm or 3.1 px of the features of the first layer between the two projections. As the algorithm is limited to integer values thus far, a 3 px shift of the sample features was assumed in the optimization process. By shifting the right projection 3 px with respect to the left projection the FZP structure is aligned in both projections and the difference image shows the contour of the Au nanoparticles (Fig. 9(f)). Thus, the theoretical shift from the sample dimensions matches well with the actual shift in the projections. The two numerically retrieved slices are presented in Figs. 9(g) and (h). The FZP nanostructures are clearly discernible in the first layer, while the Au nanoparticles are attributed to the second layer. This finding aligns with the qualitative impression highlighted by the corresponding anaglyph (see Fig. 9(d)). As the separation into only two layers is merely a rough approximation of the actual 3D representation of the sample volume, the disentangling of the Au nanoparticles from the FZP is not yet optimal and faint contributions from the other layer's content remain visible in the images. One could describe stereo ptychography as a case of limited angle tomography with a significant missing wedge. For this reason a full 3D reconstruction of a volumetric sample is not possible. Nevertheless, further enhancements to the algorithm may facilitate more precise layer separation. The outcomes illustrate that two sample layers with a distance of only 480 nm can be effectively distinguished through stereo X-ray ptychography. Since the recovery of the two layers is based on the individually reconstructed phase images, one could in principle also apply this concept to sequentially recorded projections.

To quantitatively recover slices from stereo X-ray projections, the sample should have a limited number of well-separated layers, two for the algorithm presented here. Prior knowledge of the layer distance is advantageous for slice recovery, but it can also be estimated from the shift of the layers visible in an anaglyph. The interlayer distance should be between the depth of field of a single beam and the depth resolution of the stereo setup. For optically thick objects the stereo-slice recovery could probably be applied to multi-slice reconstructions offering the opportunity to recover even more layers.

5. Conclusion

This proof of principle experiment is the first demonstration of stereoscopic ptychography in the hard X-ray regime. By simultaneous scanning with multiple inclined nanobeams, in the presented example of a microchip, one is able to visually separate various electronic layers with an substantially improved depth resolution. Since the total thickness of the layered electronic structure is only 3.8 µm it underlines the submicron axial resolution of our stereoscopic, hard X-ray microscope that is well below the limits of multi-slice single-beam ptychography. It is therefore comparable to high-performance multi-layer X-ray optics [56] at, however, less restrictive experimental conditions of a larger working distance between optics and sample.

For measurements that rely on shorter acquisition times, especially *in-situ* or *operando* studies, our technique has the unique potential to acquire a depth impression of a sample with a single scan.

Stereo X-ray ptychography improves the depth of field by one order of magnitude in comparison to multi-slice ptychography using similar nanofocusing optics. In the future, we expect that further developments will enable one to separate even more sample layers. In this way, a good volumetric representation of a layered sample will be obtained from only 2D scanning data.

Funding. Bundesministerium für Bildung und Forschung (05K20GUA); Vetenskapsrådet (2019-06104); Deutsche Forschungsgemeinschaft (426888090); Helmholtz Association (HIDSS-0002 (DASHH)).

Acknowledgments. This work was supported by the Bundesministerium für Bildung und Forschung (BMBF) within the Röntgen-Ångström-Cluster via the project 05K2020-2019-06104 XStereoVision (grant no. 05K20GUA) and the Swedish Research council with grant number 2019-06104. S.R. acknowledges funding from the Deutsche Forschungsgemeinschaft (DFG) - SFB 1441 - Project-ID 426888090. J.H. and J.D. are funded by Hi-Acts, an innovation platform under the grant of the HGF. J.D. received financial support from grant HIDSS-0002 DASHH (Data Science in Hamburg - Helmholtz Graduate School for the Structure of Matter). We acknowledge DESY (Hamburg, Germany), a member of the Helmholtz Association HGF, for the provision of experimental facilities. Parts of this research were carried out at PETRA III and we would like to thank Dennis Brückner and Jan Garrevoet for assistance in using beamline P06. We thank Stephan Botta, Ralph Döhrmann, and Patrik Wiljes for the design of the necessary adaptations of PtyNAMi and their implementation. Furthermore, we acknowledge Lukas Grote and Hanna Ohlin for their support in pre-studies. We thank Satishkumar Kulkarni from the DESY Nanolab for the FIB-SEM image of the microchip. This research was supported in part through the Maxwell computational resources operated at DESY.

Disclosures. The authors declare no conflicts of interest.

Data availability. Data underlying the results presented in this paper are not publicly available at this time but may be obtained from the authors upon reasonable request.

Supplemental document. See Supplement 1 for supporting content.

References

1. L. E. Franken, K. Grünewald, E. J. Boekema, *et al.*, "A technical introduction to transmission electron microscopy for soft-matter: Imaging, possibilities, choices, and technical developments," Small **16**(14), 1906198 (2020).
2. J. Miao, T. Ishikawa, I. K. Robinson, *et al.*, "Beyond crystallography: Diffractive imaging using coherent X-ray light sources," Science **348**(6234), 530–535 (2015).
3. F. Pfeiffer, "X-ray ptychography," Nat. Photonics **12**(1), 9–17 (2018).
4. J. M. Rodenburg and H. M. L. Faulkner, "A phase retrieval algorithm for shifting illumination," Appl. Phys. Lett. **85**(20), 4795–4797 (2004).
5. P. Thibault, M. Dierolf, O. Bunk, *et al.*, "Probe retrieval in ptychographic coherent diffractive imaging," Ultramicroscopy **109**(4), 338–343 (2009).
6. A. M. Maiden and J. M. Rodenburg, "An improved ptychographical phase retrieval algorithm for diffractive imaging," Ultramicroscopy **109**(10), 1256–1262 (2009).
7. A. Schropp, P. Boye, A. Goldschmidt, *et al.*, "Non-destructive and quantitative imaging of a nano-structured microchip by ptychographic hard X-ray scanning microscopy," J. Microscopy **241**(1), 9–12 (2011).
8. A. Schropp, R. Hoppe, J. Patommel, *et al.*, "Hard X-ray scanning microscopy with coherent radiation: Beyond the resolution of conventional X-ray microscopes," Appl. Phys. Lett. **100**(25), 253112 (2012).
9. M. Dierolf, A. Menzel, P. Thibault, *et al.*, "Ptychographic X-ray computed tomography at the nanoscale," Nature **467**(7314), 436–439 (2010).
10. M. Holler, M. Guizar-Sicairos, E. H. R. Tsai, *et al.*, "High-resolution non-destructive three-dimensional imaging of integrated circuits," Nature **543**(7645), 402–406 (2017).
11. M. Holler, M. Odstrcil, M. Guizar-Sicairos, *et al.*, "Three-dimensional imaging of integrated circuits with macro- to nanoscale zoom," Nat. Electron. **2**(10), 464–470 (2019).
12. A. M. Maiden, M. J. Humphry, and J. M. Rodenburg, "Ptychographic transmission microscopy in three dimensions using a multi-slice approach," J. Opt. Soc. Am. A **29**(8), 1606–1614 (2012).
13. E. H. R. Tsai, I. Usov, A. Diaz, *et al.*, "X-ray ptychography with extended depth of field," Opt. Express **24**(25), 29089 (2016).

14. M. Kahnt, L. Grote, D. Brückner, *et al.*, "Multi-slice ptychography enables high-resolution measurements in extended chemical reactors," Sci. Rep. **11**(1), 1500 (2021).
15. M. Holler, A. Diaz, M. Guizar-Sicairos, *et al.*, "X-ray ptychographic computed tomography at 16 nm isotropic 3D resolution," Sci. Rep. **4**(1), 3857 (2014).
16. S. Gleber, C. Knöche, J. Thieme, *et al.*, "3-D computer reconstruction of x-ray microscopy objects from stereo images," J. Phys. IV France **104**, 639–642 (2003).
17. S.-C. Gleber, J. Sedlmair, M. Bertilson, *et al.*, "X-ray stereo microscopy for investigation of dynamics in soils," J. Phys.: Conf. Ser. **186**, 012104 (2009).
18. T. Kimura, Y. Takeo, K. Sakurai, *et al.*, "Soft X-ray ptychography system using a wolter mirror for achromatic illumination optics," Opt. Express **30**(15), 26220 (2022).
19. K. Shimomura, A. Suzuki, M. Hirose, *et al.*, "Precession X-ray ptychography with multislice approach," Phys. Rev. B - Condens. Matter Mater. Phys. **91**(21), 214114 (2015).
20. K. Shimomura, M. Hirose, and Y. Takahashi, "Multislice imaging of integrated circuits by precession X-ray ptychography," Acta Crystallogr. A Found Adv. **74**(1), 66–70 (2018).
21. C. Chang, X. Pan, H. Tao, *et al.*, "3D single-shot ptychography with highly tilted illuminations," Opt. Express **29**(19), 30878 (2021).
22. D. Goldberger, J. Barolak, C. G. Durfee, *et al.*, "Three-dimensional single-shot ptychography," Opt. Express **28**(13), 18887 (2020).
23. M. Hoshino, K. Uesugi, J. Pearson, *et al.*, "Development of an X-ray real-time stereo imaging technique using synchrotron radiation," J. Synchrotron Radiat. **18**(4), 569–574 (2011).
24. W. Voegeli, K. Kajiwara, H. Kudo, *et al.*, "Multibeam X-ray optical system for high-speed tomography," Optica **7**(5), 514 (2020).
25. W. Voegeli, H. Takayama, X. Liang, *et al.*, "Multibeam x-ray tomography optical system for narrow-energy-bandwidth synchrotron radiation," Appl. Phys. Express **17**(3), 032002 (2024).
26. E. M. Asimakopoulou, V. Bellucci, S. Birnsteinova, *et al.*, "Development towards high-resolution kHz-speed rotation-free volumetric imaging," Opt. Express **32**(3), 4413 (2024).
27. J. Duarte, R. Cassin, J. Huijts, *et al.*, "Computed stereo lensless X-ray imaging," Nat. Photonics **13**(7), 449–453 (2019).
28. D. Fainozzi, M. Ippoliti, F. Bille, *et al.*, "Three-dimensional coherent diffraction snapshot imaging using extreme-ultraviolet radiation from a free electron laser," Optica **10**(8), 1053 (2023).
29. P. Villanueva-Perez, B. Pedrini, R. Mokso, *et al.*, "Hard X-ray multi-projection imaging for single-shot approaches," Optica **5**(12), 1521 (2018).
30. P. Villanueva-Perez, V. Bellucci, Y. Zhang, *et al.*, "Megahertz X-ray multi-projection imaging," arXiv (2023).
31. V. Bellucci, M.-C. Zdora, L. Mikeš, *et al.*, "Hard X-ray stereographic microscopy for single-shot differential phase imaging," Opt. Express **31**(11), 18399 (2023).
32. S. Flenner, A. Kubec, C. David, *et al.*, "Dual-beam x-ray nano-holotomography," J. Synchrotron Radiat. **31**(4), 916–922 (2024).
33. K. Kharitonov, M. Mehrjoo, M. Ruiz-Lopez, *et al.*, "Single-shot ptychography at a soft x-ray free-electron laser," Sci. Rep. **12**(1), 14430 (2022).
34. T. Li, M. Kahnt, T. L. Sheppard, *et al.*, "X-ray multibeam ptychography at up to 20 kev: Nano-lithography enhances x-ray nano-imaging," Adv. Sci. **11**(30), 2310075 (2024).
35. M. Hirose, T. Higashino, N. Ishiguro, *et al.*, "Multibeam ptychography with synchrotron hard x-rays," Opt. Express **28**(2), 1216 (2020).
36. M. Lyubomirskiy, F. Wittwer, M. Kahnt, *et al.*, "Multi-beam x-ray ptychography using coded probes for rapid non-destructive high resolution imaging of extended samples," Sci. Rep. **12**(1), 6203 (2022).
37. Y. Yao, Y. Jiang, J. A. Klug, *et al.*, "Multi-beam x-ray ptychography for high-throughput coherent diffraction imaging," Sci. Rep. **10**(1), 19550 (2020).
38. F. Wittwer, M. Lyubomirskiy, F. Koch, *et al.*, "Upscaling of multi-beam x-ray ptychography for efficient x-ray microscopy with high resolution and large field of view," Appl. Phys. Lett. **118**(17), 171102 (2021).
39. J. Deng, C. Preissner, J. A. Klug, *et al.*, "The Velociprobe: An ultrafast hard X-ray nanoprobe for high-resolution ptychographic imaging," Rev. Sci. Instrum. **90**(8), 083701 (2019).
40. J. Reinhardt, R. Hoppe, G. Hofmann, *et al.*, "Beamstop-based low-background ptychography to image weakly scattering objects," Ultramicroscopy **173**, 52–57 (2017).
41. R. N. Wilke, M. Priebe, M. Bartels, *et al.*, "Hard X-ray imaging of bacterial cells: nano-diffraction and ptychographic reconstruction," Opt. Express **20**(17), 19232–19254 (2012).
42. S. Baier, C. D. Damsgaard, M. Scholz, *et al.*, "In situ ptychography of heterogeneous catalysts using hard X-rays: High resolution imaging at ambient pressure and elevated temperature," Microsc. Microanal. **22**(1), 178–188 (2016).
43. L. Grote, M. Seyrich, R. Döhrmann, *et al.*, "Imaging Cu_2O nanocube hollowing in solution by quantitative in situ X-ray ptychography," Nat. Commun. **13**(1), 4971 (2022).
44. L. Grote, S.-A. Hussak, L. Albers, *et al.*, "Multimodal imaging of cubic Cu_2O@Au nanocage formation via galvanic replacement using X-ray ptychography and nano diffraction," Sci. Rep. **13**(1), 318 (2023).
45. C. Jacobsen, "Relaxation of the Crowther criterion in multislice tomography," Opt. Lett. **43**(19), 4811 (2018).

46. H. Ohlin, T. Frisk, M. Åstrand, *et al.*, "Miniaturized sulfite-based gold bath for controlled electroplating of zone plate nanostructures," Micromachines **13**(3), 452 (2022).
47. M. Åstrand, T. Frisk, H. Ohlin, *et al.*, "Understanding dose correction for high-resolution 50 kV electron-beam lithography on thick resist layers," Micro and Nano Eng. **16**, 100141 (2022).
48. A. Schropp, R. Döhrmann, S. Botta, *et al.*, "PtyNAMi: ptychographic nano-analytical microscope," J. Appl. Crystallogr. **53**(4), 957–971 (2020).
49. F. Wittwer, R. Hoppe, F. Seiboth, *et al.*, "Ptychography with a virtually enlarged illumination," Microsc. Microanal. **24**(S2), 48–49 (2018).
50. M. Odstrcil, M. Holler, and M. Guizar-Sicairos, "Arbitrary-path fly-scan ptychography," Opt. Express **26**(10), 12585 (2018).
51. F. Wittwer, J. Hagemann, D. Brückner, *et al.*, "Phase retrieval framework for direct reconstruction of the projected refractive index applied to ptychography and holography," Optica **9**(3), 295 (2022).
52. J. Hagemann, A.-L. Robisch, D. R. Luke, *et al.*, "Reconstruction of wave front and object for inline holography from a set of detection planes," Opt. Express **22**(10), 11552–11569 (2014).
53. C. Homann, T. Hohage, J. Hagemann, *et al.*, "Validity of the empty-beam correction in near-field imaging," Phys. Rev. A **91**(1), 013821 (2015).
54. A. Schropp, R. Hoppe, V. Meier, *et al.*, "Full spatial characterization of a nanofocused x-ray free-electron laser beam by ptychographic imaging," Sci. Rep. **3**(1), 1633 (2013).
55. B. Henke, E. Gullikson, and J. Davis, "X-ray interactions: Photoabsorption, scattering, transmission, and reflection at e = 50-30,000 ev, z = 1-92," At. Data Nucl. Data Tables **54**(2), 181–342 (1993).
56. S. Bajt, M. Prasciolu, H. Fleckenstein, *et al.*, "X-ray focusing with efficient high-NA multilayer laue lenses," Light: Sci. Appl. **7**(3), 17162 (2017).